

Large-scale dynamics in visual quorum sensing chiral suspensions

Yuxin Zhou¹, Qingqing Yin¹, Shubhadip Nayak², Poulami Bag², Pulak K. Ghosh², Yunyun Li^{1,*}, Fabio Marchesoni^{1,3}

¹ MOE Key Laboratory of Advanced Micro-Structured Materials,
School of Physics Science and Engineering, Tongji University, Shanghai 200092, China

² Department of Chemistry, Presidency University, Kolkata 700073, India and

³ Dipartimento di Fisica, Università di Camerino, I-62032 Camerino, Italy*

(Dated: August 18, 2025)

Motility-induced phase separation is an efficient aggregation mechanism of active matter, yet biological systems exhibit richer organization through communication among constituents. We investigate suspensions of active particles that change chirality when neighbor density within their visual cone exceeds a threshold - a communication-based non-reciprocal interaction akin to quorum sensing. Tuning the visual cone triggers programmable transitions—from disorder to phase separation to hyperuniformity. Notably, phase separation triggers large-scale circulation, with robust edge currents persistently flowing around dense clusters, while particle distributions inside become effectively hyperuniform. These are genuine non-reciprocal effects which occur even in the absence of steric interactions. Remarkably, in active-passive mixtures, only 5% quorum-sensing chiral particles suffice to induce collective circulation. Thus, simple perception-based rules can generate life-like order, offering design principles for programmable active materials and micro-robotic swarms.

Introduction

Our understanding of how the microscopic details of the single-particle dynamics lead to different collective behaviors is presently far from satisfactory. For this reason, researchers started investigating non-reciprocal interactions as a tool to model spontaneous clustering in active matter [1–3]. Non-reciprocity refers to a scenario where a particle influences the motion of others without experiencing any reaction in return. Non-reciprocal interactions do not necessarily require attractive force fields [4–6] or reciprocal pairwise potentials [7], nor do they encompass the steric effects [8, 9] responsible for motility-induced phase separation (MIPS) [10]. Indeed, self-propelled particles may aggregate by adjusting their velocity according to the perceived direction and the local density of their peers, a mechanism known in biology as *quorum sensing* (QS) [11, 12].

Quorum sensing in active suspensions is known to produce intriguing clustering effects. Bechinger and coworkers showed that disordered swarms can form when individual particles switch off self-propulsion either in regions of high peer concentration, independently of their relative orientation [13], or, on reverse, when their sensing cone points toward low peer density regions [14]. We agree to refer to the latter case as *visual* QS. More complex chiral QS protocols have been invoked to generate rotating swarms, or swirls [15–20].

Another unresolved question is that current MIPS models fall short in capturing the collective dynamics of chiral swimmers [21]. Chirality is an essential property of active matter. The circular and helical trajectories executed by many biological microorganisms, like bacteria and algae, on fluid surfaces or in chemical gradients, regulate both their individual and collective functionalities [22], like foraging and biofilm growth. On the other hand,

fabrication imperfections in the geometry, mass density, or catalytic coating of a synthetic swimmer can result in a (possibly unwanted) torque, which makes it a chiral active particle. Liao and Klapp [23] and Ma and Ni [24] demonstrated that, when the torques are sufficiently large, the dynamics of chiral active suspensions in two dimensions (2D) is drastically modified: multiple clusters arise from the competition of the MIPS mechanism, producing cohesion, and large-scale circulating currents, causing disintegration.

In this study, we explore the collective particle circulation in a chiral active suspension by complementing (or entirely replacing) the steric pair interactions considered in Ref. [24] with long-range, non-reciprocal interactions. To avoid the interplay with MIPS cohesion, we numerically simulated the dynamics of strongly chiral particles with gyration radius smaller than the average suspension mean-free path: QS protocols were implemented to either toggle the chirality on and off or reverse its sign based on the local density within a limited visual cone. Focusing on the latter protocol, we observed that, by tuning the chirality of individual particles, visual QS can generate large-scale mass circulation in the form of localized edge currents. Unlike the mechanism described in Ref. [24], such currents encircle high-density particle aggregates. As the sensing range expands, the density of these clusters decreases until they are eventually replaced by nearly empty cavities, also surrounded by edge currents but with an opposite sign. Ultimately, the suspension transitions to an effective hyperuniform state [25]. Hyperuniformity (HU) [26, 27] characterizes the particles distribution also within the largest clusters at lower sensing ranges. More remarkably, we noticed that, in contrast with MIPS, such large-scale collective dynamics occurs even in the absence of steric interactions, i.e., for pointlike particles, as a genuine visual QS effect. When examining a mixture of passive and QS chiral particles, we found that even a small fraction of the latter is suffi-

* yunyunli@tongji.edu.cn

cient to produce persistent edge currents. These currents are robust enough to “herd” passive particles together, forming dense structures similar to those observed in fully chiral suspensions. This finding not only reinforces the role of edge currents in shaping two-phase structures, but also points to potential applications in active matter manipulation and micro-robotics.

Results

Model

In 2D, the center of mass, $\mathbf{r}_i = (x_i, y_i)$, of an overdamped active disk of index i executes a time-correlated Brownian motion of Langevin equations (see Materials and Methods)

$$\dot{\mathbf{r}}_i = \mathbf{v}_{0i}, \quad \dot{\theta}_i = \omega_i + \sqrt{D_\theta} \xi_{\theta i}(t). \quad (1)$$

Here, the modulus of its self-propulsion vector, $\mathbf{v}_{0i} = v_0(\cos \theta_i, \sin \theta_i)$, is constant, while its orientation with respect to the longitudinal x -axis, θ_i , fluctuates subjected to the stationary, delta-correlated noise source $\xi_{\theta i}(t)$, with $\langle \xi_{\theta i}(t) \xi_{\theta j}(0) \rangle = 2\delta_{ij}\delta(t)$. The particle chiral frequency, ω_i , is allowed to switch between two fixed values according to the QS protocol detailed below.

We numerically simulated a chiral suspension by randomly placing N identical, independent Janus disks of Eq. (1) in a square box of side L and imposing periodic boundary conditions. Effects due to the particle finite size were modeled by the Weeks-Chandler-Andersen (WCA) pair potential [28], $V_{ij} = 4\epsilon[(\sigma/r_{ij})^{12} - (\sigma/r_{ij})^6 + 1/4]$, if $r_{ij} \leq r_m$, and $= 0$, otherwise, where $r_m = 2^{1/6}\sigma$, $\epsilon = 1$, $i, j = 1, \dots, N$ are the pair labels, and $\sigma = 2r_0$ was taken as the “nominal” disk diameter. The average packing fraction of the suspension is $\bar{\phi} = \pi r_0^2 \rho_0$, with $\rho_0 = N/L^2$ denoting its average density. Further reciprocal interactions and hydrodynamical interactions [29, 30], have been neglected.

We then assumed that the chirality of the tagged particle depends on the spatial distribution of its neighbors. Without entering the details of specific sensing mechanisms [11, 12, 31, 32], we defined the sensing function of particle i as [13]

$$P_i(d_c) = \sum_{j \in V_i^{d_c}} 1/(2\pi r_{ij}), \quad (2)$$

where $V_i^{d_c}$ is its “visual cone” with axis parallel to \mathbf{v}_{0i} , radius (or sensing range) d_c , and semi-aperture α [Fig. 1(a)]. The particle chirality is then governed by the simple *QS protocol*,

$$\omega_i = \begin{cases} \omega_+ & P_i(d_c) \leq P_{\text{th}} \\ \omega_- & P_i(d_c) > P_{\text{th}} \end{cases} \quad (3)$$

with QS threshold $P_{\text{th}} = (\alpha/\pi)\rho_0 L_p$ [33]. The focus of this report is on protocol 1: $\omega_+ = -\omega_- = \omega_0$, with tunable $\omega_0 \geq 0$. Numerical results for protocol 2: $\omega_+ = 0$

and $\omega_- = -\omega_0$, are reported for a comparison (see Sec. S1 of Supplementary Text). As shown in Ref. [19], ω_i can be regulated by tuning the misalignment between \mathbf{v}_{0i} and the particle’s visual cone axis. Of course, reversing the sign of ω_0 does not change the qualitative description of the suspension collective dynamics. Note that for a uniform suspension the sensing function of Eq. (2) is approximatively $\bar{P}(d_c) = (\alpha/\pi)\rho_0(d_c - \sigma)$. Clearly, this form of particle interaction is non-reciprocal.

Monodisperse suspensions

We started simulating a uniformly distributed active suspension with $\omega_i = \omega_+$, and packing fraction, $\bar{\phi}$, small enough to rule out conventional MIPS [35, 36]. We set ω_0 large enough for the particle gyration radius, $r_\omega = v_0/\omega_0$, to be much smaller than the mean free path in a uniformly distributed achiral suspension, $l_c = \pi r_0/2\bar{\phi}$. As detailed in Materials and Methods, under this assumption, the ratio d_c/L_p , which characterizes the range and strength of the QS interaction, is the only relevant control parameter involving the length scales in the model. In the absence of additional long-range interactions, the suspension distribution remains randomly uniform [21]. On applying QS protocol 1, its collective dynamics changes dramatically (Figs. 1 and 2). On increasing the sensing range beyond a certain threshold, d_c^* [its dependence on $\bar{\phi}$ is illustrated in Fig. 1(f)], the particle distribution grows inhomogeneous, with the formation first of multi-cluster patterns and, then, of cavities. Contrary to conventional MIPS, with increasing d_c the stationary particle density in the regions surrounding the cluster structures and inside the cavities tends to vanish, whereas the density inside the clusters decreases, i.e., clusters grow in size [Figs. 1(b)-(e), see also Fig. 2(a)-(d)]. Accordingly, the transition from cluster to cavity configurations inside a finite simulation box is marked by extended periodic structures [Fig. 1(c)] (see also Sec. S3 of Supplementary Text), which appear for d_c values independent of the system size. On further increasing d_c , cavities shrink until they vanish and the suspension turns hyperuniform [25]. Furthermore, we remark that the transient time for the suspension to achieve its steady state diverges with its size, N (see discussion of Fig. S9). The dependence of the configuration of a finite-size suspension on the sensing range under protocol 1 and 2 is illustrated in Fig. 1(h). There we used the fraction of particles that underwent chirality change, η , as a quantitative indicator. Under protocol 2, no phase separation occurs and HU emerges after about 50% of the particles have turned chiral. In stark contrast with the uniform configurations from both protocols, particle diffusion in the presence of two-phase structures is mostly anomalous (see Sec. S2 of Supplementary Text).

From a more quantitative viewpoint, we remark that for the QS protocols of Eq. (3) to describe a collective mechanism involving three or more JP’s, the sensing function of Eq. (2) for a colliding pair, $P_p(\sigma) = 1/(2\pi\sigma)$, must be smaller than P_{th} , that is $\bar{\phi} > \phi_{\text{QS}}$ with $\phi_{\text{QS}} =$

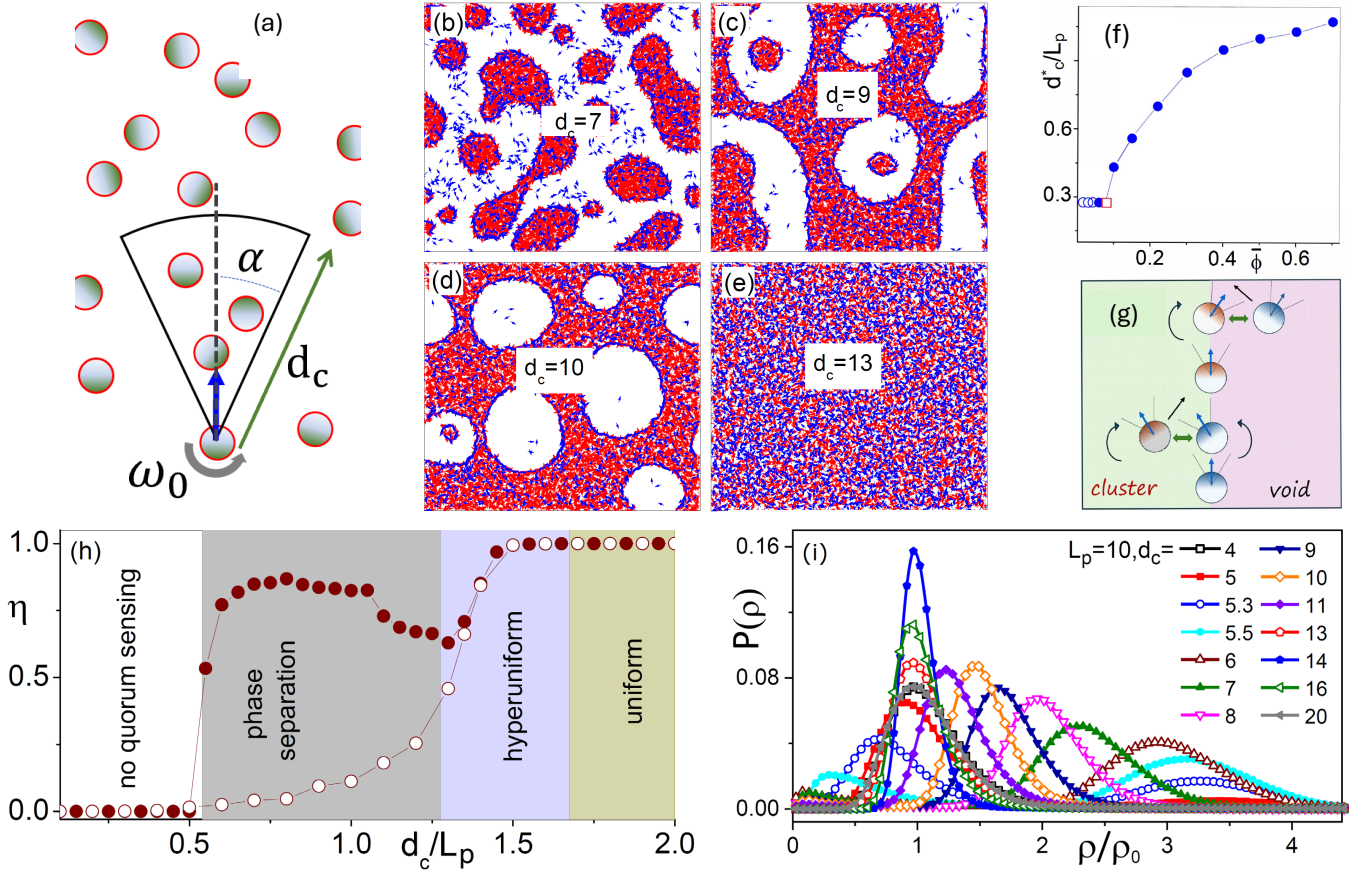


FIG. 1. Configurations of a chiral suspension of $N = 10^4$ Janus hard disks of radius $r_0 = 1$, speed $v_0 = 0.5$ and persistence time $\tau_\theta = 100$; the simulation box size, L , corresponds to the average packing fraction $\bar{\phi} = 0.15$. (a) Particle's QS visual cone, $V_i^{d_c}$, introduced in Eq. (2). (b)-(e) Suspension snapshots at $t = 3 \cdot 10^4$ for QS protocol 1 with $L_p = 10$, $\alpha = \pi/2$, $\omega_0 = 1$, and different d_c (see legends) (see also Fig. S6). Arrows of different colors denote the orientation of the self-propulsion vectors, \mathbf{v}_{0i} , of particles with positive (blue) and negative (red) chirality. (f) Clustering threshold d_c^* vs. $\bar{\phi}$ for the model parameters of (b)-(e): filled circles correspond to the appearance of the $\rho > \rho_0$ peak in the $P(\rho)$ curves in (i); the red square denotes the critical point (ϕ_{QS}, d_{QS}) introduced in the text; empty circles mark the appearance of chirality switches in the absence of clusters. (g) Schematic of the QS-induced edge current mechanism (see text). (h) Fraction of particles with chirality ω_- , η , vs. d_c in a suspension with $N = 10^4$ and $\bar{\phi} = 0.15$. η was computed starting at $t > 5 \cdot 10^4$ and averaged 250 times at intervals of 200 time units under protocol 1 (filled circles) and 2 (empty circles). (i) Distribution of the local suspension density, ρ , for different d_c (see legend) computed by means of the Voronoi polygon method [34] and time averaged over 500 snapshots taken 200 time units apart, starting at $t = 10^5$. Note that the higher-density peak (dense phase) emerges abruptly at $d_c \simeq 5.3$, and shifts toward ρ_0 as d_c increases. In contrast, the lower-density peak (dilute phase) shifts toward 0, until it disappears entirely at $d_c \simeq 13$.

$(\pi/4\alpha)(r_0/L_p)$. Moreover, since the disk diameter is finite, the further condition, $d_c > d_{QS} = \sigma$, applies, consistently with the data displayed in Fig. 1(f). The formation of clusters for $d_c > d_c^*$ is marked by the appearance of a second peak in the $P(\rho)$ curves of Fig. 1(i), centered around a local density value, ρ_c , larger than ρ_0 . Note that η may be positive even for $\bar{\phi} < \phi_{QS}$, i.e., particles may switch chirality without forming clusters. Particles inside large clusters [$0.6 < d_c/L_p < 1$ in Fig. 1(h)], look uniformly distributed, so that ρ_c can be estimated by equating $\bar{P}(d_c)$ with P_{th} , hence $\rho_c = \rho_0 L_p / (d_c - \sigma)$, in fairly good agreement with the simulation data, e.g., of Fig. 2(e). This means that here, contrary to MIPS, the

density of the dense phase does not remain constant at varying the control parameter, d_c . This argument is less accurate for small clusters, where a relatively larger fraction of particles appears to move along the boundaries in dense files. By the same token we anticipate that for $d_c - \sigma \gtrsim L_p$ local particle density inhomogeneities are no longer required for the tagged particle to satisfy the QS condition Eq. (3). This yields a working estimate for the d_c value where two-phase configurations disappear and HU sets in ($d_c/L_p \gtrsim 1.3$ for the suspension of Fig. 1). Based on this argument, the transition to HU is expected to be independent of the simulation box' size.

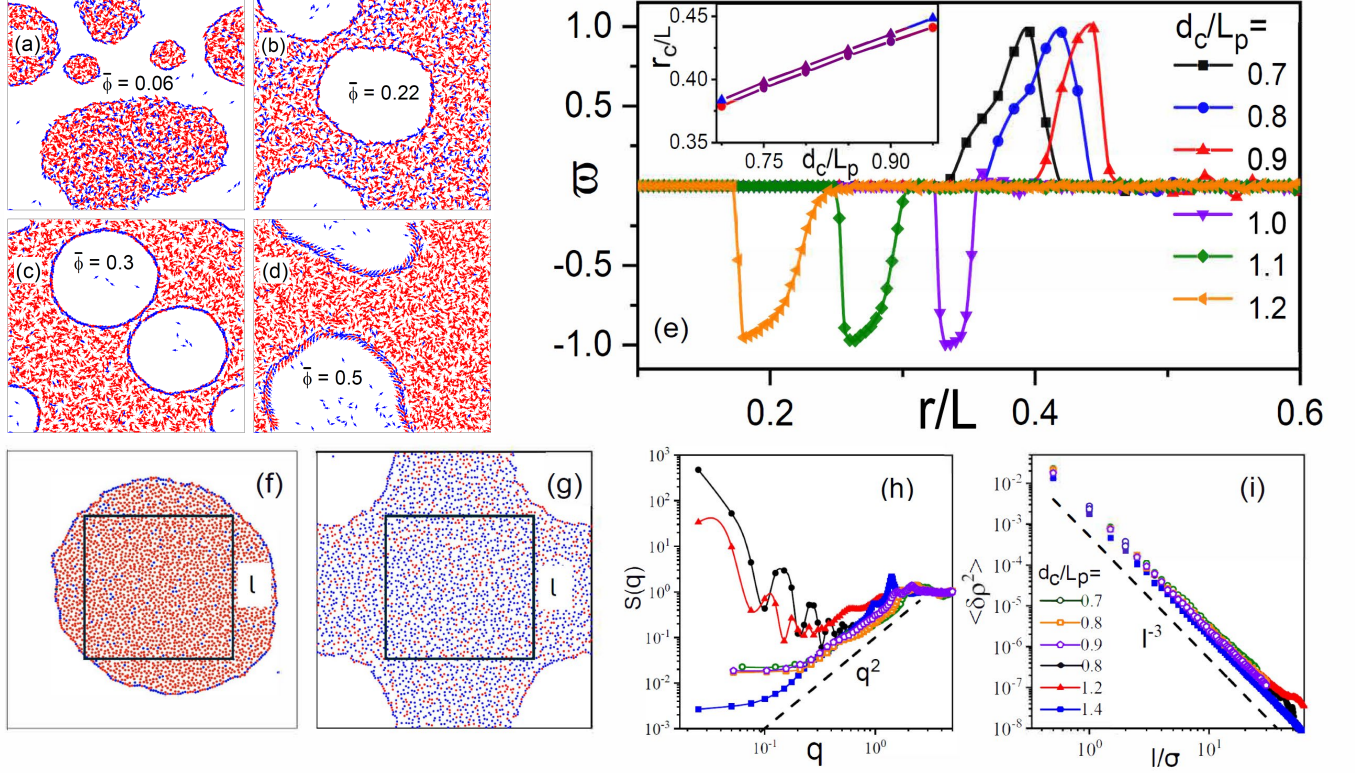


FIG. 2. Edge currents in two-phase configurations of a chiral suspension of $N = 3 \cdot 10^3$ Janus disks under QS protocol 1. (a)-(d) suspension snapshots at $t = 3 \cdot 10^4$ for different $\bar{\phi}$ (see legends); arrow color code as in Fig. 1. Disk parameters: $r_0 = 1$, $v_0 = 0.5$, and $\tau_0 = 100$; QS protocol parameters: $d_c = 8$, $L_p = 10$, $\alpha = \pi/2$, and $\omega_0 = 1$. For better visualization, refer to the movies in Supplementary Material. (e) Vorticity, ϖ vs r , for $\bar{\phi} = 0.15$ [positive for clusters ($d_c = 7, 8, 9$) and negative for cavities ($d_c = 10, 11, 12$)], time averaged over 500 snapshots taken 200 time units apart, starting at $t = 10^6$. All other parameters are as in (a)-(d); r is measured from the cluster (cavity) centroid. Inset: maximum of $\varpi(r)$, r_c , vs d_c for $N = 3 \cdot 10^3$ (blue symbols) and $N = 6 \cdot 10^3$ (red symbols). (f)-(i) Hyperuniformity in the above chiral suspension with $N = 3 \cdot 10^3$ and $\bar{\phi} = 0.15$ under QS protocol 1. (f),(g) Stationary configurations respectively for $d_c = 8$ (cluster) and 10 (cavity). The black squares denote the area where the HU quantifiers in (h) and (i) were computed (we remind for a comparison that here $L = 250$). (h) $S(q)$ and (i) $\langle \delta \rho^2(l) \rangle$ for different d_c in dense phase regions (empty symbols) and over the entire simulation box (filled symbols). The suppression of the $S(q)$ decay at very low q is a noise effect (see Sec. S4.F of Supplementary Text). Time averages: over 1,000 snapshots taken 200 time units apart, starting at $t = 5 \cdot 10^4$.

Edge currents and hyperuniformity

As anticipated above, cluster and cavity structures are delimited by edge currents, which, for $\omega_0 > 0$, flow counterclockwise (clockwise) along the cluster (cavity) boundaries. In stationary configurations, when almost all particles aggregated into large clusters or the cavities are empty, boundary particle circulation involves one or more layers, their number increasing with $\bar{\phi}$ [Figs. 2(a)-(d)]. This happens only for QS protocol 1, as sketched in Fig. 1(g). Suppose that a disk moves along the divide between a dense region on the left and an empty one on the right. If the peer concentration inside its visual cone is relatively low, it will rotate counterclockwise, until it point inside the dense region. At this point, according to QS protocol 1, it reverses its chirality sign and starts rotating clockwise. As its visual cone finally points toward

the empty region, it switches back to its initial (positive) chiral state, and the cycle repeats itself. For the particles in the dense region and sufficiently away from the edge, the condition $P_i(d_c) > P_{th}$ is always satisfied, they all keep rotating clockwise on-site (their diffusivity is minimal) and, therefore, appear to be brought together by one or more moving boundary layers. This simple argument explains stationarity and orientation of the edge currents for QS protocol 1 with appropriately restricted visual aperture, $0.4 \lesssim \alpha/\pi \lesssim 0.8$ (see Sec. S4.B of Supplementary Text), their absence for QS protocol 2, and implies that particles flowing along the boundary layers change chirality sign with frequency of the order of ω_0 . All of this is in good agreement with our simulation results (see movies in Supplementary Material).

A more quantitative analysis of the edge currents was

performed by computing the vorticity function $\varpi(r)$ [Fig. 2(e)] (see Materials and Methods). As expected, for $\omega_0 > 0$, the vorticity is positive for clusters and negative for cavities. However, it is non-zero only in a narrow annulus of radius $r \sim r_c$, which delimits the structure boundary, consistently with the notion of edge current. We also observed that the clusters' size, measured by r_c , is proportional to L and grows almost linearly with d_c/L_p [Fig. 2(e), inset], in correspondence with the decrease of ρ_c in Fig. 1(i) (see Sec. S4.C of Supplementary Text for more details). Finally, by equating the cluster diameter, $2r_c$, to the box size, L , we get an estimate of the L -independent d_c value, when, in the two-phase configurations, clusters get replaced by cavities [that is $d_c/L_p \gtrsim 1$ for the suspension of Fig. 2(e)].

The emergence of HU [27] was anticipated in Fig. 1(i): Upon increasing d_c , the high ρ peak of the local density distributions eventually disappears and the peak centered around ρ_0 shrinks with respect to the corresponding (Gaussian) peak at very low/high d_c . To better illustrate the HU properties of our system, we computed the (time averaged) structure factor, $S(q) = (1/N) \sum_{i,j=1}^N \exp(i\mathbf{q} \cdot [\mathbf{r}_i - \mathbf{r}_j])$, and density variance, $\langle \delta\rho^2(l) \rangle = \langle [\rho(l) - \langle \rho(l) \rangle]^2 \rangle$, of the stationary suspension in observation windows of size l [Figs. 2 (f),(g)]. For $1.3 < d_c/L_p < 1.6$, we obtained clear-cut scaling laws, $S(q \rightarrow 0) \sim q^2$ [Fig. 2(h)], and $\langle \delta\rho^2(l \rightarrow \infty) \rangle \sim l^{-3}$ [Fig. 2(i)]. Consistently with the discussion in Ref. [21], we interpret these results as the signature of strong HU, the closest to a perfect crystal structure. Within this d_c range, HU spans the entire simulation box. For smaller d_c values, we analyzed the particle distributions inside the two-phase structures, clusters and cavities, alike. Restricting the computation of $S(q)$ and $\langle \delta\rho^2(l) \rangle$ to observation windows located inside the dense phase [e.g., the large cluster and cavity of Figs. 2(f),(g)] does not change the exponents of the above scaling laws. It should be noted that $S(q \rightarrow 0)$ is small but finite. As discussed in Sec. S4.F of Supplementary Text (compare Figs. S10 and S11), this behavior arises mostly from the randomness inherent to the visual QS function of Eq. (2), and is therefore markedly suppressed in suspension setups involving larger sensing ranges, d_c . We consider this to be an example of *effective* HU [21].

Chiral-passive mixtures

To investigate the role of steric interactions in the present context, we simulated a colloidal mixture containing only a small fraction, δ , of *strongly* chiral JP's. Active and passive disks have the same radius, and interact with each other via the WCA potential. A weak translational noise term with $D_0 \ll D_s$ (see Sec. S4.A of Supplementary Text) was incorporated to enhance the model's realism, though it is not critical to the subsequent analysis.

The QS threshold of Eq.(2) should now be interpreted as follows: (i) QS applies exclusively to active particles; (ii) the summation in Eq. (2) is limited to passive parti-

cles within the visual cone defined by parameters α and d_c . Accordingly, the chirality of a tagged active particle remains unchanged even in the presence of neighboring active particles, and the QS threshold can be rewritten as $P_{\text{th}} = (\alpha/\pi)\rho_p L_p$, where ρ_p is the average density of the passive component in the mixture.

Our numerical findings for such a selective QS protocol are illustrated in Fig. 3. A striking observation is that at sufficiently large sensing distances, the mixture develops spatial inhomogeneity, marked by the emergence of multiple clusters. These structures feature a central core of passive particles enveloped by one or more counterclockwise-rotating layers of active particles. The stability and orientation of the edge currents align with the mechanisms sketched in Fig. 1(g). Notably, even a modest proportion of active particles (5% or less, see Fig. S8) proves sufficient to densely "herd" passive colloids into compacted aggregates.

Key trends evident in Fig. 3 include:

- (i) Increasing d_c enlarges cluster size, causing the surrounding dilute regions to contract and eventually fragment into predominantly empty cavities encircled by clockwise-oriented edge currents. This behavior, consistent with observations in the monodisperse suspensions of Figs. 1 and 2, coincides with gradual melting of the cluster core. Concurrently, the particle arrangement transitions sequentially from hexagonal crystalline to hexatic and ultimately disordered.
- (ii) Raising δ amplifies cluster multiplicity and accelerates clustering onset at smaller d_c . This stems from the combined dynamics of a greater number of visual QS disks, which reorganize more rapidly into rotating boundary layers, resulting in smaller colloidal "herds." Additionally, at fixed d_c , higher δ increases the number of active boundary layers while reducing in-cluster particle density.
- (iii) Smaller visual angles α are favored. Comparison of snapshots in Fig. 3 reveals that for $\alpha = \pi/4$, clusters are more abundant, structurally denser, and surrounded by thicker active shells compared to $\alpha = \pi/2$. Consequently, the transition from clustered to cavity configurations occurs at reduced d_c . Furthermore, simulations conducted for $\alpha = \pi$ (representing the full visual cone or regular QS) reveal that passive disks, as well as levo- and dextrogyre disks, tend to separate. In agreement with the reasoning illustrated in Fig. 1(g), regions occupied by passive particles are not surrounded by edge currents. The spatial arrangements of the mixture following this dynamical separation display are depicted in Fig. 3 (bottom row).

Discussion

The most intriguing aspect of the collective dynamics in a visual QS chiral suspension is that chirality changes of individual JPs, characterized by a small gyration radius, can translate into large-scale dynamical effects involving large portions of the suspension, namely edge currents and strong HU. An additional effect of this mechanism is the enhancement of particle diffusivity under HU condi-

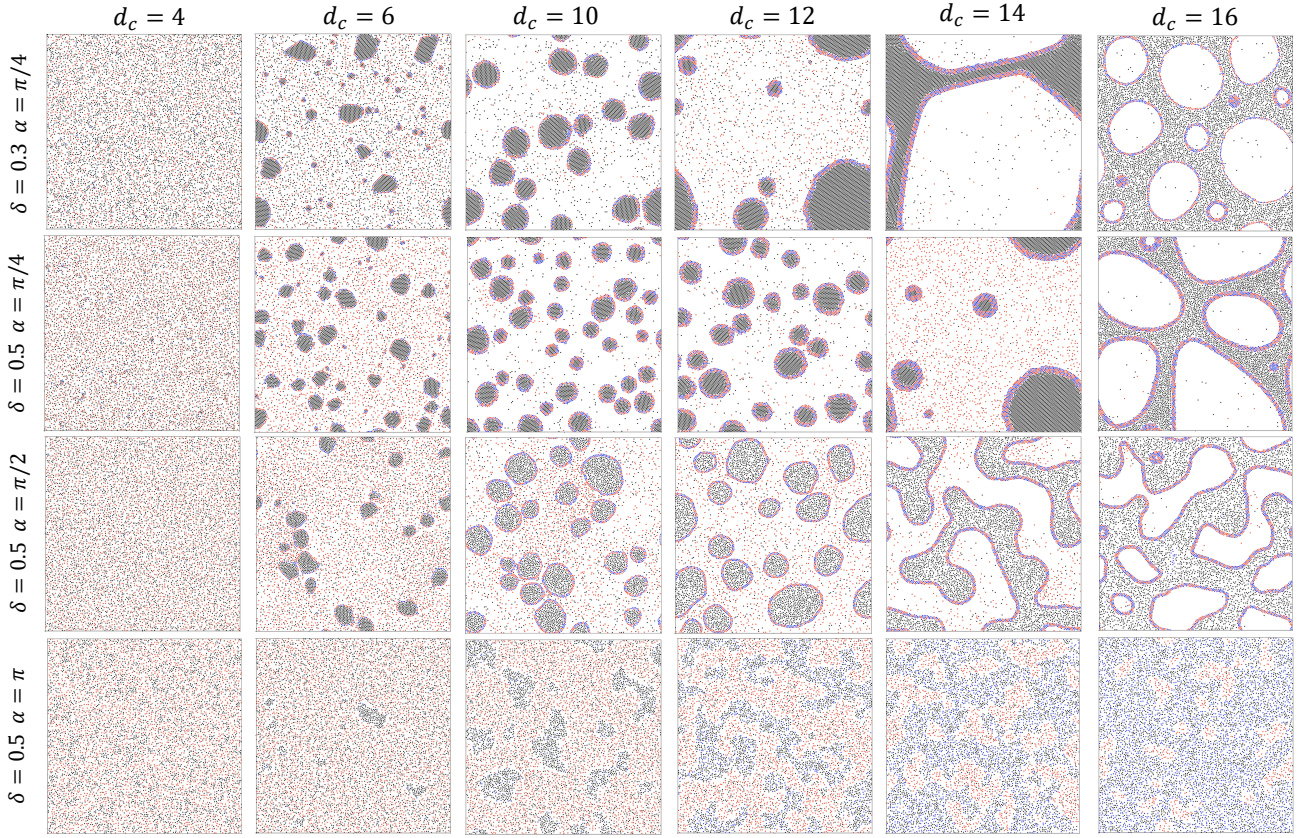


FIG. 3. Aggregation of passive particles by chiral particles under QS protocol 1 of Eq. (3) (implemented as explained in the text) for different δ , α , and d_c (see legends) and in the presence of thermal fluctuation with $D_0 = 0.01$. δ is the fraction of active particles [blue (red) denoting positive (negative) chirality]; all the remaining (black) particles are passive. Disk parameters: $r_0 = 1$, $v_0 = 1$, and $D_\theta = 0.01$; suspension parameters: $N = 6 \cdot 10^3$, $\phi = 0.21$, $\epsilon = 1$; other QS protocol parameters: $L_p = 10$, $\omega_0 = 1$. Snapshots taken at $t = 5 \cdot 10^4$.

tions, well above its expected free-particle value. In Sec. S4.E, we also checked the robustness of the reported effects against variations of the parameters modeling the JP disk self-propulsion (v_0 and D_θ), the QS protocol (α and ω_0) and the pair potential (σ and ϵ).

Moreover, edge currents constitute a genuine QS phenomenon which can arise even without steric interactions. This conclusion is supported by numerical simulations showing that dense structures surrounded by persistent edge currents form spontaneously despite deactivating the WCA potential (i.e., setting the interaction strength $\epsilon = 0$, see Sec. S4 of Supplementary Text). Stated otherwise, the interfacial boundaries surrounding these condensed regions do not generate confining pressure on the enclosed particles. The chirality-based segregation of particles therefore originates not from excluded-volume interactions, but rather emerges through a dynamical mechanism inherent the adopted visual QS protocol. In contrast, herding of passive particles by QS chiral particles occurs only in the presence of steric interactions between the two particle species. Indeed, numerical simulation show that, under the action of translational noise and in the

absence of steric repulsion, passive disks would traverse undisturbed the encircling edge currents, thus restoring spatial uniformity.

Materials and Methods

The suspension was assumed to be athermal. Accordingly, in Eq. (1) we neglected thermal fluctuations against the angular noise due to the self-propulsion mechanism [37]. The strength of the angular noise, D_θ , defines the persistence (or correlation) time, $\tau_\theta = 1/D_\theta$, and length, $l_\theta = v_0/D_\theta$, of a free self-propelled disk. We remind that, for $t \gg \tau_\theta$, a free JP of fixed chiral frequency, ω_0 , would undergo (non-Gaussian) normal diffusion with diffusion constant $D_c = D_s/[1 + (\omega_0\tau_\theta)^2]$, where $D_s = v_0^2/2D_\theta$ is the diffusion constant of its achiral counterpart [38]. The stochastic differential Eqs. (1) were numerically integrated by means of a standard Euler-Maruyama scheme [39]. To ensure numerical stability, the numerical integrations have been performed using an appropriately short time step not larger than $\delta t = 10^{-3}$.

The vorticity function displayed in Fig. 2(e), is de-

defined as $\varpi(r) = [1/N(r)] \sum_{i=1}^{N(r)} \varphi_i/|\varphi_i|$, where $\varphi_i = (\mathbf{r}_i - \mathbf{r}_\times) \times \mathbf{v}_i/|\mathbf{r}_i - \mathbf{r}_\times|^2$ and $N(r)$ is the number of particles with assigned distance from the structure centroid, $r < |\mathbf{r}_i - \mathbf{r}_\times| < r + dr$. This quantity was computed by choosing N and t so as to obtain single large clusters or cavities, rounded in shape and with an easily identifiable centroid, \mathbf{r}_c [see Fig. 2(f),(g)].

Averages of $\varpi(r)$, $S(q)$ and $\delta\rho^2(l)$ where computed over hundreds of steady-state configurations taken 200 time units apart. [see caption of Fig. 2].

The values of the length scales introduced in the Model section were chosen based on practical considerations:

(i) The disk radius, r_0 in the V_{ij} potential, was assumed to be much smaller than the average inter-particle separation, $l_L = (\pi r_0^2/\bar{\phi})^{1/2}$ (quasi-pointlike particle regime). Note that edge currents are detectable also in the absence of steric repulsion.

(ii) The gyration radius, $r_\omega = v_0/\omega_0$, was taken to be much smaller than the mean free path in a uniformly distributed achiral suspension, $l_c = \pi r_0/(2\bar{\phi})$. This ensures that the chiral MIPS mechanism described in Ref. [21] does not come into play, avoiding unnecessary complications.

(iii) To make the chiral nature of the active Janus disks experimentally detectable, we required $\tau_\theta\omega_0 \gg 1$, or equivalently, that r_ω be much smaller than the persistence length, $l_\theta = v_0\tau_\theta$.

(iv) The QS protocol involves two more lengths, the sensing range, d_c , and the threshold defining range, L_p [P_{th} in Eq. (3)]. As shown in Fig. 1(f), the emergence of collective QS effects requires that the sensing range, d_c , be comparable to or larger than l_L .

(v) As a consequence of condition (iv), edge currents become detectable only when $r_\omega \lesssim l_L$ (see Fig. S6). We note that below the MIPS threshold value of $\bar{\phi}$ [36], which is assumed throughout this work, it holds that $l_c < l_L$. This imposes a tighter constraint on r_ω (an upper bound) and correspondingly on ω_0 (a lower bound), compared to condition (ii).

(vi) Finally, the box size L is not explicitly stated in the figure captions, as it is determined by our choice of the system size N , the average packing fraction $\bar{\phi}$, and the disk radius r_0 .

r_0 and v_0 , which are held constant throughout the simulations, simply define the units of length and time. Therefore, among all the length scales listed above, only r_ω , and l_L (i.e., ω_0 , $\bar{\phi}$) play a significant role in this study; d_c (in units of L_p) quantifies the strength of the QS interaction. The other scales, l_c and l_θ , are set to be much larger than l_L .

References

- [1] S. Jiang and S. Granick, *Janus particle synthesis, self-assembly and applications* (RSC Publishing, Cambridge, 2012).
- [2] A. Walther and A. H. E. Müller, Janus particles: Synthesis, self-assembly, physical properties, and applications, *Chem. Rev.* **113**, 5194 (2013).
- [3] M. C. Marchetti, J. F. Joanny, S. Ramaswamy, T. B. Liverpool, J. Prost, M. Rao, and R. A. Simha, Hydrodynamics of soft active matter, *Rev. Mod. Phys.* **85**, 1143 (2013).
- [4] R. Jayaram, Y. Jie, L. Zhao, and H. I. Andersson, Clustering of inertial spheres in evolving Taylor-Green vortex flow, *Phys. Fluids* **32**, 043306 (2020).
- [5] Y. Li, Y. Zhou, F. Marchesoni, and P. K. Ghosh, Colloidal clustering and diffusion in a convection cell array, *Soft Matter* **18**, 4778 (2022).
- [6] P. K. Ghosh, Y. Zhou, Y. Li, F. Marchesoni, and F. Nori, Binary mixtures in linear convection arrays, *ChemPhysChem* **24**, e202200471 (2023).
- [7] Y. Duan, J. Agudo-Canalejo, R. Golestanian, and B. Mahault, Dynamical pattern formation without self-attraction in quorum-sensing active matter: The interplay between nonreciprocity and motility, *Phys. Rev. Lett.* **131**, 148301 (2023).
- [8] Y. Fily and M. C. Marchetti, Athermal phase separation of self-propelled particles with no alignment, *Phys. Rev. Lett.* **108**, 235702 (2012).
- [9] G. S. Redner, M. F. Hagan, and A. Baskaran, Structure and dynamics of a phase-separating active colloidal fluid, *Phys. Rev. Lett.* **110**, 055701 (2013).
- [10] M. E. Cates and J. Tailleur, Motility-induced phase separation, *Annu. Rev. Condens. Matter Phys.* **6**, 219 (2015).
- [11] M. B. Miller and B. L. Bassler, Quorum sensing in bacteria, *Annu. Rev. Microbiol.* **55**, 165 (2001).
- [12] M. R. Parsek and E. P. Greenberg, Sociomicrobiology: the connections between quorum sensing and biofilms, *Trends Microbiol.* **13**, 27 (2005).
- [13] T. Bäuerle, A. Fischer, T. Speck, and C. Bechinger, Self-organization of active particles by quorum sensing rules, *Nat. Commun.* **9**, 3232 (2018).
- [14] F. A. Lavergne, H. Wendehehne, T. Bäuerle, and C. Bechinger, Group formation and cohesion of active particles with visual perception-dependent motility, *Science* **364**, 6435 (2019).
- [15] L. Barberis and F. Peruani, Large-scale patterns in a minimal cognitive flocking model: Incidental leaders, nematic patterns, and aggregates, *Phys. Rev. Lett.* **117**, 248001 (2016).
- [16] T. Bäuerle, L. R. C., and C. Bechinger, Formation of stable and responsive collective states in suspensions of active colloids, *Nat. Commun.* **11**, 2547 (2020).
- [17] S. Thapa, B.-E. Pinchasik, and Y. Shokef, Emergent clustering due to quorum sensing in active matter, *New J. Phys.* **26**, 023010 (2024).
- [18] Y. Zhou, Y. Li, and F. Marchesoni, A quorum sensing active matter in a confined geometry, *Chin. Phys. Lett.* **40**, 100505 (2023).
- [19] R. Saavedra, G. Gompper, and M. Ripoll, Swirling due to misaligned perception-dependent motility, *Phys. Rev. Lett.* **132**, 268301 (2024).
- [20] R. S. Negi, R. G. Winkler, and G. Gompper, Emergent collective behavior of active brownian particles with visual perception, *Soft Matter* **18**, 6167 (2022).
- [21] Q. Lei, M. P. Ciamarra, and R. Ni, Nonequilibrium strongly hyperuniform fluids of circle active particles with large local density fluctuations, *Sci. Adv.* **5**, eaau7423 (2019).
- [22] E. Lauga and T. R. Powers, The hydrodynamics of swimming microorganisms, *Rep. Prog. Phys.* **72**, 096601 (2009).

- [23] G.-J. Liao and S. H. L. Klapp, Clustering and phase separation of circle swimmers dispersed in a monolayer, *Soft Matter* **14**, 7873 (2018).
- [24] Z. Ma and R. Ni, Dynamical clustering interrupts motility-induced phase separation in chiral active brownian particles, *J. Chem. Phys.* **156**, 021102 (2022).
- [25] Q. Lei and R. Ni, Hydrodynamics of random-organizing hyperuniform fluids, *Proc. Natl. Acad. Sci. U. S. A.* **116**, 22983 (2019).
- [26] S. Torquato and F. H. Stillinger, Local density fluctuations, hyperuniformity, and order metrics, *Phys. Rev. E* **68**, 041113 (2003).
- [27] S. Torquato, Hyperuniform states of matter, *Phys. Rep.* **745**, 1 (2018).
- [28] J. D. Weeks, D. Chandler, and H. C. Andersen, Role of repulsive forces in determining the equilibrium structure of simple liquids, *J. Chem. Phys.* **54**, 5237 (1971).
- [29] X. Yang, C. Liu, Y. Li, F. Marchesoni, P. Hänggi, and H. P. Zhang, Hydrodynamic and entropic effects on colloidal diffusion in corrugated channels, *Proc. Natl. Acad. Sci. U.S.A.* **114**, 9564 (2017).
- [30] D. Takagi, J. Palacci, A. B. Braunschweig, M. J. Shelley, and J. Zhang, Hydrodynamic capture of microswimmers into sphere-bound orbits, *Soft Matter* **10**, 1784 (2014).
- [31] F. Berlinger, M. Gauci, and R. Nagpal, Implicit coordination for 3d underwater collective behaviors in a fish-inspired robot swarm, *Sci Robot.* **6**, eabd8668 (2021).
- [32] M. Jiang, A. Zhou, R. Chen, Y. Yang, H. Dong, and W. Wang, Collective motions of fish originate from balanced local perceptual interactions and individual stochastic, *Phys. Rev. E* **107**, 024411 (2023).
- [33] Y. Zhou, Y. Li, and F. Marchesoni, Clustering of quorum sensing colloidal particles, *Natl. Sci. Open* **3**, 20230081 (2024).
- [34] A. Okabe and K. Sugihara, *Spatial Tessellations: Concepts and Applications of Voronoi Diagrams* (2nd ed. (Wiley, New York), 2000).
- [35] G. S. Redner, M. F. Hagan, and A. Baskaran, Structure and dynamics of a phase-separating active colloidal fluid, *Phys. Rev. Lett.* **110**, 055701 (2013).
- [36] S. Nayak, P. Bag, P. K. Ghosh, Y. Li, Y. Zhou, Q. Yin, F. Marchesoni, and F. Nori, Diffusion transients in motility-induced phase separation, *Phys. Rev. Res.* **7**, 013153 (2025).
- [37] P. K. Ghosh, V. R. Misko, F. Marchesoni, and F. Nori, Self-propelled janus particles in a ratchet: Numerical simulations, *Phys. Rev. Lett.* **110**, 268301 (2013).
- [38] S. van Teeffelen and H. Löwen, Dynamics of a brownian circle swimmer, *Phys. Rev. E* **78**, 020101 (2008).
- [39] P. E. Kloeden and E. Platen, *Numerical Solution of Stochastic Differential Equations* (Springer, Berlin, 1992).

Acknowledgements

Funding: This work is supported by National Natural Science Foundation of China grant 12375037 (LYY), National Natural Science Foundation of China grant 12350710786 (MF, LYY), SERB Core Research Grant CRG/2021/007394 (GPK), CSIR EMR II file no. 01/3115/23 (GPK), UGC, New Delhi, India Senior Research Fellowship (BP). **Author contributions:** LYY, GPK and MF designed the research; ZY, YQ, NS and BP performed research; All authors contributed to the data analysis; MF wrote the manuscript; GPK and LYY edited it. **Competing interests:** The authors declare that they have no competing interests. **Data and materials availability:** All data needed to evaluate the conclusions in the paper are presented in the paper and/or Supplementary Materials. Additional data related to this paper may be requested from the authors.